



Improved inversion of aerosol components in the atmospheric column from remote sensing data

Ying Zhang¹, Zhengqiang Li¹, Yu Chen², Gerrit de Leeuw^{1,3}, Chi Zhang¹, Yisong Xie¹, and Kaitao Li¹

¹Aerospace Information Research Institute, Chinese Academy of Sciences, Beijing 100101, China

²Public Meteorological Service Center, China Meteorological Administration, Beijing 100081, China

³R&D Satellite Observations, Royal Netherlands Meteorological Institute (KNMI), 3730AE De Bilt, the Netherlands

Correspondence: Zhengqiang Li (lizq@radi.ac.cn)

Received: 18 November 2019 – Discussion started: 22 January 2020

Revised: 10 August 2020 – Accepted: 23 September 2020 – Published: 4 November 2020

Abstract. Knowledge of the composition of atmospheric aerosols is important for reducing uncertainty in climate assessment. In this study, an improved algorithm is developed for the retrieval of atmospheric columnar aerosol components from optical remote sensing data. This is achieved by using the complex refractive index (CRI) of a multicomponent liquid system in the forward model and minimizing the differences with the observations. The aerosol components in this algorithm comprise five species, combining eight sub-components including black carbon (BC), water-soluble organic matter (WSOM) and water-insoluble organic matter (WIOM), ammonium nitrate (AN), sodium chloride (SC), dust-like content (DU), and aerosol water content in the fine and coarse modes (AW_f and AW_c). The calculation of the CRI in the multicomponent liquid system allows for the separation of the water-soluble components (AN, WSOM and AW_f) in the fine mode and SC and AW_c in the coarse mode. The uncertainty in the retrieval results is analyzed based on the simulation of typical models, showing that the complex refractive index obtained from instantaneous optical-physical inversion compares well with that obtained from chemical estimation. The algorithm was used to retrieve the columnar aerosol components over China using the ground-based remote sensing measurements from the Sun-sky radiometer Observation NETwork (SONET) in the period from 2010 to 2016. The results were used to analyze the regional distribution and interannual variation. The analysis shows that the atmospheric columnar DU component is dominant in the northern region of China, whereas the AW is higher in the southern coastal region. The SC component retrieved over the desert in northwest China originates from a pale-

omarine source. The AN significantly decreased from 2011 to 2016, by 21.9 mg m^{-2} , which is inseparable from China's environmental control policies.

1 Introduction

Atmospheric aerosol consists of a suspension of solid and/or liquid particles in the air. The chemical composition and mixing state of the aerosol particles affect their optical characteristics, which in turn influence the energy budget of the Earth-atmosphere system and thus climate (Boucher et al., 2013).

To measure aerosol composition, many methods are used including online analysis in the field, sample analysis in the laboratory and remote sensing estimation. Each technique provides information on the aerosol composition which may differ in content and detail. Because of fast observation and low cost, the application of remote sensing techniques to estimate aerosol composition has developed rapidly since 2000. Satheesh and Srinivasan (2002), Satheesh et al. (1999, 2002), and Satheesh and Krishna (2005) established an algorithm for the inversion of aerosol components from remote sensing data based on the hypothesis of external mixing and assuming fixed size distributions for each component. But an external mixture usually cannot accurately describe the natural state of aerosols. Even if the particles are individually pure when first produced, numerous processes in the atmosphere will convert an external mixture to an internal mixture (Lesins et al., 2002). Therefore, internal-mixing hypotheses are widely used and multiple approaches have been developed (e.g., Schuster et al., 2005, 2009, 2016; Arola et al.,

2011; Z. Li et al., 2013; L. Li et al., 2019; Wang et al., 2013; van Beelen et al., 2014; Zhang et al., 2018). Schuster et al. (2005) determined the volume fraction of black carbon in an internal mixture with water and a soluble component by fitting the calculated complex refractive index to retrieved AERONET values at all four available wavelengths. In a follow-up study, Schuster et al. (2009) applied a similar procedure to determine the aerosol water fraction by fitting the real part of the refractive index of an internal mixture of water and soluble and insoluble species to observations by minimizing the cost function at all four wavelengths together. In this work the ratio of the dry volume fraction of insoluble aerosols to that of soluble aerosols was constrained by using a climatological value and the real refractive index which also prescribes the aerosol hygroscopicity. This constraint also provides a maximum insoluble fraction and the fraction of dust aerosol. Brown carbon was further estimated by Arola et al. (2011) due to the large change in its absorbing characteristics with wavelength for wavelengths smaller than 550 nm, but the dust component was ignored in this study. Aerosol bimodal characteristics were used by Schuster et al. (2016) to estimate the aerosol-absorbing components including BC, brown carbon and hematite in the fine and coarse modes. This method was also embedded in the GRASP (Generalized Retrieval of Aerosol and Surface Properties; Dubovik et al., 2011) system by L. Li et al. (2019) for application to POLDER PARASOL observations. The above algorithms are aimed at retrieving absorbing aerosol components, such as BC, brown carbon and iron oxides, but have only simple treatment for scattering components, especially the host of multicomponent liquids.

Van Beelen et al. (2014) introduced water-soluble organic matter (WSOM) in the inversion process based on the hygroscopicity of the organic matter (OM) mixture, but in this study water-insoluble organic matter (WIOM) was not accounted for. Some studies separated the OM based only on the spectral changes (Xie et al., 2017; Choi and Ghim, 2016), leading to large uncertainty in the results. Zhang et al. (2018) simultaneously retrieved the WSOM and WIOM components but ignored the error in the refractive index introduced by the aerosol volume averaging method applied to the multicomponent liquid system. For other nonabsorbing components, the water content and inorganic components in the fine mode are identified by the difference in hygroscopic growth between organic and inorganic matter (Zhang et al., 2018; van Beelen et al., 2014). In the coarse mode, sea salt is identified by the aerosol sphericity in the study of Xie et al. (2017), but this parameter is difficult to observe.

Although the retrieval of aerosol components by using remote sensing methods has been greatly developed, the application of hygroscopicity to identify the weak and nonabsorbing components in a multicomponent liquid system remains difficult. In the current study, hygroscopicity is introduced to solve for the refractive index in a multicomponent liquid system. The results are used in the algorithm to retrieve aerosol

components from data obtained from the ground-based remote sensing network SONET (Sun–sky radiometer Observation NETwork; Li et al., 2018). The data and method are described in Sects. 2 and 3, respectively. The results for the aerosol components are presented and analyzed in Sect. 4, and we conclude this study in Sect. 5.

2 Measurements

2.1 Sun–sky radiometer

The multiwavelength polarized sun–sky radiometer CE318-DP manufactured by Cimel Electronique in France, as an accurate instrument designed for long-term continuous observations in the field, can automatically measure solar and sky radiation. It consists of an optical head, a control box and a biaxial stepping-motor system. The optical head has two views: one for direct solar radiation with no focusing lens and the other for sky radiation with a focusing lens. The internal optical system consists of a spectral and a polarizing filter to measure radiation in different wavebands with polarization directions. The nine wavebands vary from visible to near-infrared wavelengths (340, 380, 440, 500, 675, 870, 936, 1020, 1640 nm) with a full width at half maximum of 10 nm. All bands provide both radiation and polarization measurements, except the 936 nm band which only measures radiation to determine the columnar water vapor. These radiation and polarization measurements can provide sufficient information to calculate the columnar aerosol optical depth (AOD) and further retrieve the aerosol microphysical parameters.

2.2 SONET

The Sun–sky radiometer Observation NETwork (SONET) is a local observation network in China for ground-based remote sensing measurements of aerosol properties (Li et al., 2018). At present, there are 16 long-term observation sites in China, which are evenly distributed over northern, southern and northwest China and the Tibetan Plateau (Fig. 1). The longest time series is provided by the Beijing station, which was established in 2009. Five more stations joined in 2011 and 2012, and the network has been gradually growing to its current size. The geographical and topographical features of the long-term sites, such as plateau, desert, hill, plain and island, are diverse, including three megacities, three islands and one plateau site (Table 1). SONET data provide sufficient variability, as regards length of time series, spatial coverage, climatic and topographic features, and aerosol properties, for the analysis of atmospheric aerosol characteristics across China.

SONET provides continuous observations of direct sun and sky radiation measured using the multiwavelength polarization sun–sky radiometer (CE318-DP), following the AERONET protocol (Li et al., 2018). Based on the inver-

Table 1. SONET sites (name, location and geographical aspects) and meteorological stations used in this study.

SONET site						Meteorological station				Geographical feature	Geographical region
Name	Abbr	Long (°)	Lat (°)	Alt (m)	Obs. period	No.*	Long (°)	Lat (°)	Alt (m)		
Lhasa	LS	91.2	29.6	3678	Mar 2016–May 2016	55591	91.1	29.7	3649	Plateau	Qinghai–Tibet
Kashgar	KS	75.9	39.5	1320	Sep 2013–Nov 2016	51709	76.0	39.5	1289	Desert	Northwest
Zhangye	ZY	100.3	38.8	1364	Aug 2012–Oct 2016	52652	100.4	38.9	1483	Desert	
Minqin	MQ	103.0	38.6	1589	Feb 2012–Oct 2016	52681	103.1	38.6	1368	Desert and hill	
Xi'an	XA	108.9	34.2	389	May 2012–Nov 2016	57039	108.9	34.2	433	Half mountain, half plain	
Beijing	BJ	116.3	40.0	59	Dec 2009–Nov 2016	54399	116.3	40.0	46	Hill (megacity)	Northern
Harbin	HrB	126.6	45.7	223	Dec 2013–Nov 2016	50953	126.8	45.8	118	Plain	
Songshan	SS	113.1	34.5	475	Dec 2013–Nov 2016	57084	113.1	34.5	1178	Mountain and hill	
Nanjing	NJ	119.0	32.1	52	Jan 2013–Jul 2016	58238	118.8	32.0	35	Plain and hill	Southern
Shanghai	SH	121.5	31.3	84	Mar 2013–Apr 2016	58362	121.5	31.4	6	Alluvial plain (megacity)	
Hefei	HF	117.2	31.9	36	Nov 2013–Nov 2016	58321	117.2	31.9	27	Hill	
Zhoushan	ZS	122.1	29.9	29	Feb 2012–Nov 2016	58477	122.1	30.0	36	Islands	
Chengdu	CD	104.0	30.6	510	Jun 2013–Jul 2016	56276	103.8	30.4	461	Basin	
Guangzhou	GZ	113.4	23.1	28	Oct 2011–Nov 2016	59287	113.3	23.2	41	Mountain, hill and plain (megacity)	
Haikou	HK	110.3	20.0	22	Mar 2014–Mar 2016	59758	110.3	20.0	64	Island	
Sanya	SY	109.4	18.3	29	Sep 2014–Nov 2016	59948	109.5	18.2	419	Island	

* No. is the meteorological station number.

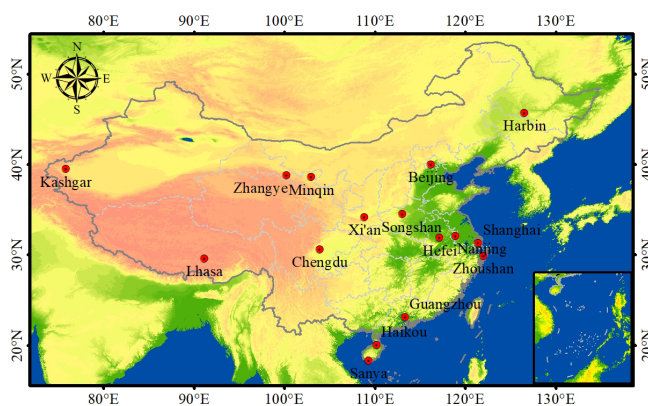


Figure 1. Locations of the 16 Sun–sky radiometer Observation NETwork (SONET) sites projected onto an elevation map of China.

sion algorithm of Dubovik and King (2000) and Dubovik et al. (2000), the 440, 675, 870 and 1020 nm wavebands are used to retrieve more than 20 parameters describing the optical, physical and chemical global properties as column-integrated properties (Li et al., 2018), including the particle volume size distribution (VSD), the complex refractive index (CRI) and aerosol components. Using these data, VSD and CRI submodal parameters of atmospheric aerosols are obtained using the modal decomposition method proposed by Zhang et al. (2017). The real parts of the CRI of the fine and coarse modes (n_f and n_c , respectively) are spectrally independent, while the imaginary parts have spectral variation at 440 nm, so they are written as $(k_{f, 440}, k_f)$ and $(k_{c, 440}, k_c)$. Using these fine- and coarse-mode characteristics of the CRI, microphysical properties of aerosols in each mode were analyzed (Z. Li et al., 2019), but the aerosol chemical components were not determined.

2.3 Meteorological data

Meteorological data provide important supplementary information for the analysis and interpretation of the SONET-retrieved aerosol information. Hourly observations from surface meteorological stations were provided by the China Meteorological Administration (CMA). Only data from manned weather stations, which are maintained regularly, were used to ensure the best possible data quality. The CMA stations closest to each SONET site were selected, and the meteorological data were collocated in time with the SONET observations by linear interpolation between the nearest observations. Figure 2 shows the statistics of the relative humidity (RH) observations at each of the 16 sites. The highest mean RH occurs at the Sanya site, and the lowest value occurs at the Lhasa site. Generally, the mean RH is relatively low at stations at northern latitudes and often also at high altitudes. The standard deviations of wet (e.g., Sanya, Haikou) and dry (e.g., Lhasa, Kashgar) sites are smaller than at other sites.

3 Methodology

The aerosol components are determined by comparison of the aerosol microphysical properties calculated using a forward model with those retrieved from the SONET observations (Zhang et al., 2017). This is achieved by minimizing the iterative kernel function, i.e., the sum of the differences between the calculated and observed properties at each of the four wavelengths together, to find the optimum solution. The forward model includes three modules: the Maxwell Garnett effective-medium approximation (Schuster et al., 2005) module to calculate aerosol internal-mixing characteristics, an aerosol hygroscopic growth module to solve the hygroscopicity of water-soluble components in a multicomponent liquid system and an organic component dynamic constraint module to keep a reasonable ratio of organic matter.

3.1 The aerosol component classification

The aerosol component classification includes five principal species (black carbon – BC, organic matter – OM, inorganic salt – IS, aerosol water content – AW, dust-like content – DU). Three of these components are further subdivided; i.e., organic matter is subdivided into water-soluble organic matter (WSOM) and water-insoluble organic matter (WIOM); inorganic salt consists of ammonium nitrate (AN) in the fine mode and sodium chloride (SC) in the coarse mode, and aerosol water content is the water content in the fine and in the coarse mode. Thus there are eight subcomponents as illustrated in Fig. 3. All of these eight aerosol components constitute a relatively complete system comparable to those used in chemical transport models.

The aerosol components are identified following three steps. The first step is the separation of the aerosol microphysical properties (VSD and CRI) into those of the fine and

coarse modes as summarized in Sect. S1 in the Supplement. For the fine-mode fraction, the water-insoluble and water-soluble components are identified using an empirical function (see Sect. 2.2.2 in Zhang et al., 2018), which describes the ratio of the water-soluble to the water-insoluble volume fractions determined by RH, together with the parameterization of aerosol soluble volume fractions by Kandler and Schütz (2007). Then the subcomponents are separated into inclusion (BC and WIOM) and their environment (AN, AW_f and WSOM) using their hygroscopic and optical absorption properties. It should be noted that the water-soluble property of aerosol components is not equivalent to hygroscopicity. Dicarboxylic acids represented by oxalic acid are dominant in the WSOM component, but their hygroscopicity is extremely low (Ma et al., 2013; Drozd et al., 2014; Jing et al., 2016). Other organic compounds in aerosols are also less hygroscopic as shown in Zhang et al. (2018, their Fig. 1). Hence, the OM components (WSOM and WIOM) are treated as nonhygroscopic components. For the coarse-mode fraction, the refractive index of the mixture (AW_c and SC) is determined by its hygroscopic growth factor. Dust and hydrate in the aerosol mixture are separated by the effective-medium approximation.

In these processes, the hygroscopic growth is determined by the hygroscopicity parameter κ and effective densities of the aerosol subcomponents, and the aerosol mixture refractive index is calculated by that of the subcomponents and the mixing state. Key parameters of the forward model and references are listed in Table 2. We notice that the effective densities for OC and DU reported from different studies cover a wide range (Ganguly et al., 2009; McConnell et al., 2008; Wagner et al., 2012; Bond and Bergstrom, 2006) because they depend on the mixing ratios. In the current study the effective density of aerosol components is used from a widely cited study by van Beelen et al. (2014).

3.2 Complex refractive index in a multicomponent liquid system

The multiple water-soluble aerosol components together with the aerosol water content make up a liquid system, with increased complexity of the calculation of hygroscopic growth and complex refractive index. The κ -Köhler theory proposed by Petters and Kreidenweis (2007) can cope with the hygroscopicity of the multicomponent liquid system. In this theory, the water activity of aqueous atmospheric particulate matter can be represented by the functional form

$$\frac{1}{a_w} = 1 + \kappa \frac{V_s}{V_w}, \quad (1)$$

where V_s is the volume of the dry particulate matter and V_w is the volume of the aerosol water content. The activity of water in solution (a_w) is close to the relative humidity (RH) due to a lower curvature effect and can therefore be replaced with RH (Tang, 1996). The hygroscopicity parameter κ is

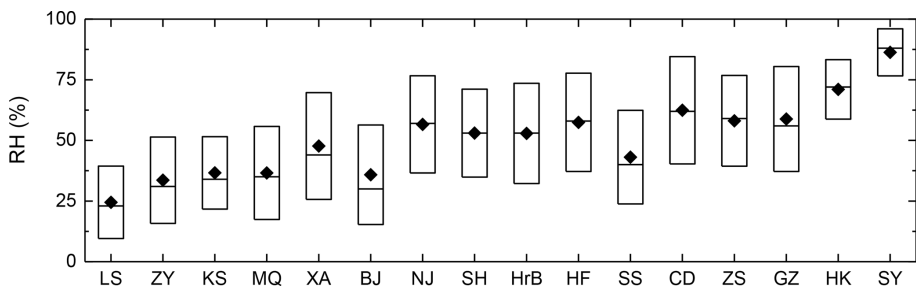


Figure 2. Boxplots of the relative humidities observed near each of the SONET sites. The observation periods for each site are shown in Table 1. The line and the diamond represent the median and mean values, respectively, and the box shows the standard deviation (1σ).

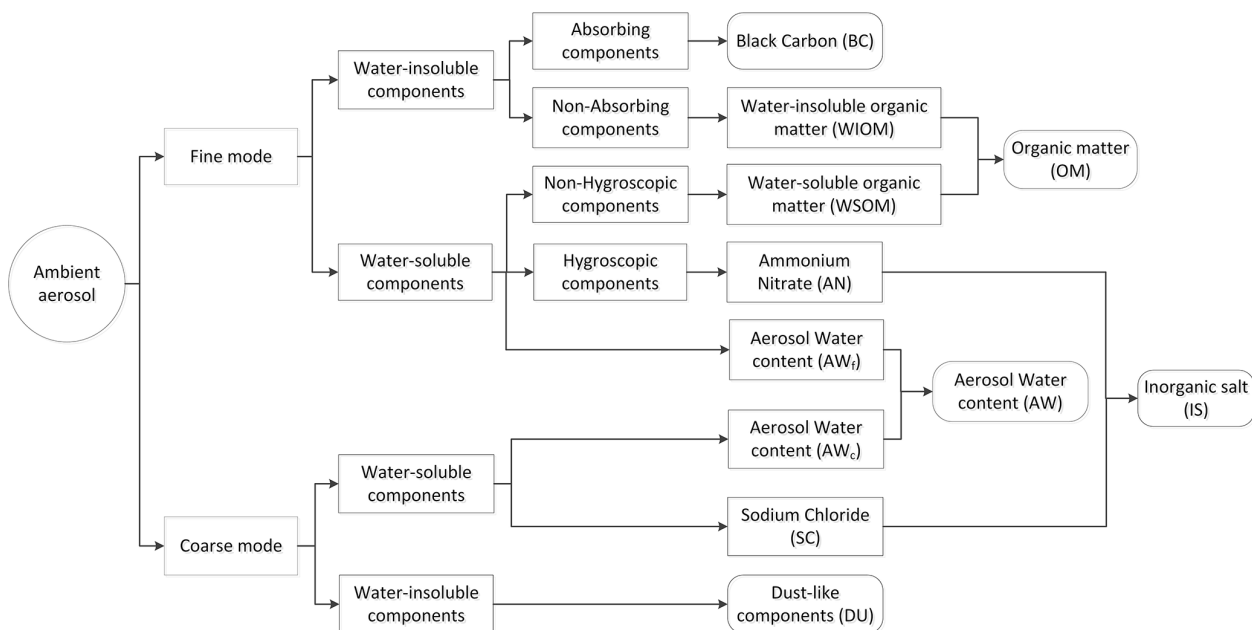


Figure 3. Aerosol component classification scheme.

defined through its effect on the water activity of the solution. In Eq. (1), the ratio of V_s to V_w can be further applied to the calculation of the volume fraction

$$\sum_i f_i = \frac{V_s}{V_s + V_w} = \frac{1 - a_w}{1 - (1 - \kappa) a_w}, \quad (2)$$

where f_i is the volume fraction of the i th component

$$f_i = \frac{V_i}{V_s + V_w}, \quad (3)$$

where V_i is the volume of the i th component.

In the multicomponent liquid system, the hygroscopicity parameter κ is given by the simple mixing rule

$$\kappa = \sum_i f_{\text{dry}, i} \kappa_i, \quad (4)$$

where κ_i is the hygroscopicity parameter of the i th component obtained from the literature (Table 2) and $f_{\text{dry}, i}$ is the

dry component volume fraction defined as

$$f_{\text{dry}, i} = \frac{V_i}{V_s}. \quad (5)$$

Using Eq. (2) for the relationship between the volume fraction and the hygroscopicity parameter, the complex refractive index of the multicomponent aerosol system can be derived using the Lorentz–Lorenz relation (Heller, 1965). Firstly, the molar refractivity (A_e) at wavelength λ can be calculated from the real part of the complex refractive index (n_i) and the volume fraction of the individual components:

$$A_e(\lambda) = \sum_i f_i A_i(\lambda). \quad (6)$$

Here A_i is the molar refractivity of the i th component represented by

$$A_i(\lambda) = \frac{n_i^2(\lambda) - 1}{n_i^2(\lambda) + 2}. \quad (7)$$

Table 2. Growth-factor-derived hygroscopicity parameter (κ), complex refractive indices ($m = n - ik$) at four wavelengths and effective density (ρ) of model components. Real and imaginary parts at four standard AERONET aerosol product wavelengths (440, 675, 870 and 1020 nm) are considered.

Component	Growth-factor- derived κ	Real part				Imaginary part		ρ (g cm ⁻³)
		n_{440}	n_{675}	n_{870}	n_{1020}	k_{440}	$k_{675-1020}$	
OM	WIOM	0.000	1.530 ^c	1.530	1.530	0.035 ^d	0.001	1.547 ⁱ
	WSOM	0.000 ^a	1.530 ^c	1.530	1.530	0.006 ^d	0.000	
AN	0.547 ^b	1.559 ^e	1.553	1.550	1.548	0.000 ^e	0.000	1.760 ^j
BC	0.000	1.950 ^f	1.950	1.950	1.950	0.790 ^f	0.790	1.800 ^j
AW	0.000	1.337 ^e	1.332	1.330	1.328	0.000 ^g	0.000	1.000 ^j
DU	0.000	1.534 ^g	1.534	1.534	1.534	0.002 ^h	0.001	2.650 ^j
SC	1.120 ^a	1.562 ^h	1.541	1.534	1.530	0.000 ⁱ	0.000	2.165 ^j

^a Petters and Kreidenweis (2007). ^b Kreidenweis et al. (2008). ^c Sun et al. (2007). ^d Chen and Bond (2010). ^e Schuster et al. (2005). ^f Bond and Bergstrom (2006). ^g Koven and Fung (2006). ^h Toon et al. (1976). ⁱ Van Beelen et al. (2014).

Then, the real and imaginary parts of the complex refractive index at wavelength λ of the multicomponent liquid system, $n_e(\lambda)$ and $k_e(\lambda)$, are obtained by using the molar refractivity and the imaginary part of the complex refractive index of the i th component (k_i), respectively.

$$n_e(\lambda) = \sqrt{\frac{1 + 2A_e(\lambda)}{1 - A_e(\lambda)}} \quad (8)$$

$$k_e(\lambda) = \sum_i f_i k_i(\lambda) \quad (9)$$

Equations (8) and (9) apply to the estimation of the complex refractive index of a multicomponent liquid system with hygroscopic growth.

3.3 Effective-medium approximation

To determine the complex refractive index of a particle, i.e., including both the multicomponent liquid system and water-insoluble matter, the complex refractive index ($m = n - ik$) at wavelength λ is expressed in terms of the permittivity, $\varepsilon(\lambda)$:

$$m(\lambda) = \sqrt{\frac{|\varepsilon(\lambda)| + Re(\varepsilon(\lambda))}{2}} + i\sqrt{\frac{|\varepsilon(\lambda)| - Re(\varepsilon(\lambda))}{2}}. \quad (10)$$

The permittivity of the multicomponent liquid system can then be calculated using Eqs. (8)–(10). Considering the water-insoluble matter in a particle as inclusion and the water-soluble matter as the environment, the permittivity of the entire aerosol particle can be obtained by the Maxwell Garnett effective-medium approximation (Schuster et al.,

2005):

$$\varepsilon_{\text{eff}}(\lambda) = \varepsilon_e + 3\varepsilon_e \left[\frac{\sum_j \frac{\varepsilon_j(\lambda) - \varepsilon_e(\lambda)}{\varepsilon_j(\lambda) + 2\varepsilon_e(\lambda)} f_j}{1 - \sum_j \frac{\varepsilon_j(\lambda) - \varepsilon_e(\lambda)}{\varepsilon_j(\lambda) + 2\varepsilon_e(\lambda)} f_j} \right], \quad (11)$$

where j is the number of water-insoluble components and $\varepsilon_j(\lambda)$ and $\varepsilon_e(\lambda)$ are the permittivities of the inclusion and its environment. The complex refractive index of the entire aerosol is estimated by the aerosol component fraction using Eq. (10).

3.4 Inversion procedure

The flowchart for the inversion of the aerosol components is shown in Fig. 4. In the fine mode, the ratio of WS and WI matter is estimated using RH as described in Sect. 2.2.2 in Zhang et al. (2018). The initial value of the host refractive index and the extreme value for the BC component are set by the calculation modules of the complex refractive index in the multicomponent liquid system (see Sect. 3.2) and the effective-medium approximation (see Sect. 3.3), respectively. In the loop to determine the BC component, two constraints are applied to separate BC from other components. The WSOM / WIOM ratio constraint was developed by Zhang et al. (2018) based on considerations published in the literature (Chalbot et al., 2016; Bougiatioti et al., 2013; Wozniak et al., 2013; Mayol-Bracero et al., 2002; Krivácsy et al., 2001; Zappoli et al., 1999):

$$\begin{cases} f_{\text{WSOM}} \cong \alpha f_{\text{WIOM}} \\ \alpha = \frac{\beta \rho_{\text{WSOM}}^{-1}}{1 - \beta \rho_{\text{WSOM}}^{-1}} \end{cases} \quad \beta \in [44\%, 77\%]. \quad (12)$$

For more detail, see Sect. 2.3.1 in Zhang et al. (2018). The volume normalization of the aerosol components in both the

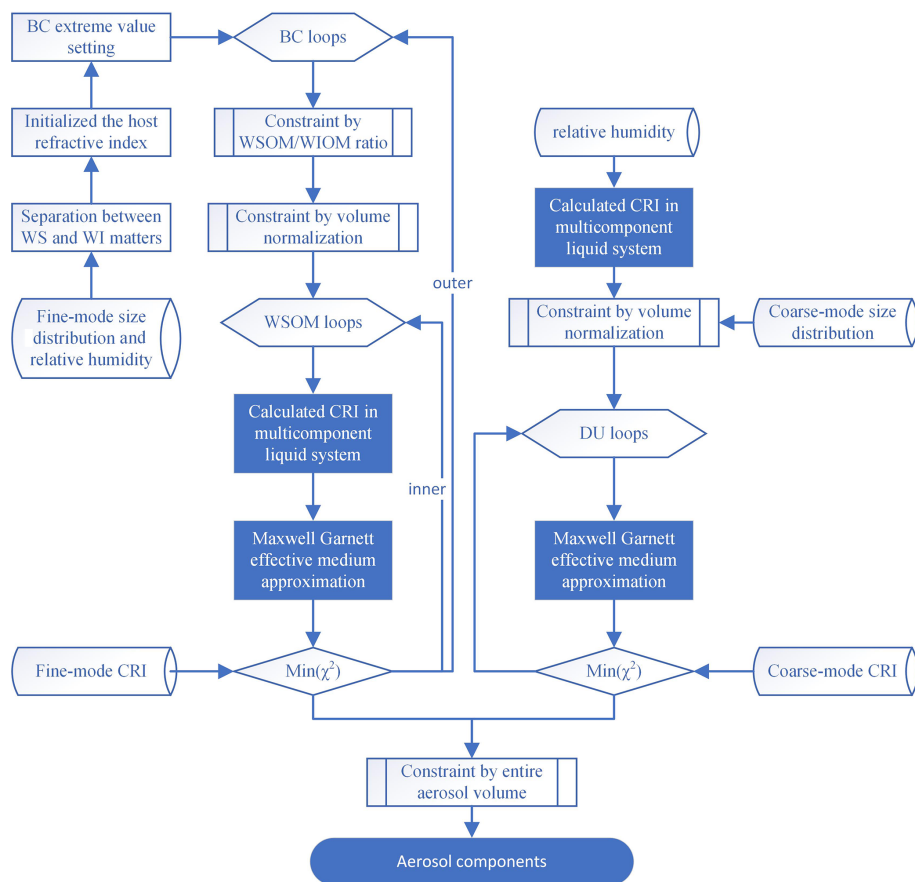


Figure 4. Flowchart of the aerosol component classification inversion algorithm.

fine and coarse modes is used to constrain the volume fraction of the aerosol components to a reasonable range (similar to in Sect. 2.3.2 in Zhang et al., 2018):

$$\left\{ \begin{array}{l} f_{\text{fine}} + f_{\text{coarse}} = 1.0 \\ f_{\text{fine}} = f_{\text{BC}} + f_{\text{AN}} + f_{\text{WSOM}} + f_{\text{WIOM}} + f_{\text{AW}_f} \\ f_{\text{coarse}} = f_{\text{DU}} + f_{\text{SC}} + f_{\text{AW}_c} . \end{array} \right. \quad (13)$$

Then the inner loop of WSOM computes the CRIs of the fine mode at different BC levels and outputs the aerosol components of minimum χ^2 . The inversion procedure for the coarse mode is simpler than that for the fine mode. There is only a loop for DU, and the complex refractive index of the host can be directly calculated by Eqs. (2)–(8) with only the input of RH. The function chi-squared (χ^2) as an iterative kernel function is expressed in the sum of the differences between the complex refractive index estimated from the forward model (m) and the retrievals (m_{rtrr}), at multiple wavelengths:

$$\chi^2 = \sum_{\lambda} \frac{(m_{\text{rtrr}}(\lambda) - m(\lambda))^2}{m_{\text{rtrr}}(\lambda)}, \quad \lambda = 440, 675, 870 \text{ and } 1020 \text{ nm.} \quad (14)$$

The retrieval is completed when the value of χ^2 reaches a minimum. The volume fractions of the aerosol components can be obtained by solving the above Eqs. (10)–(12). The aerosol mass concentration in the atmospheric column is calculated using the volume and effective density of the aerosol components.

The retrieval algorithm described here is an improvement over that described in Zhang et al. (2018). In the previous algorithm, the WSOM component was added to the host, but it could only be considered as a nonhygroscopic component. The proportions of solute and solution in the host mixture at different relative humidities should be measured in the laboratory, which limits the choice of aerosol components in the inversion process. Also, the real part of the CRI of the host was calculated by volume averaging, which can introduce a small error. The improved algorithm described here is more suitable for the calculation of the properties of a mixture of multiple water-soluble components as long as the hygroscopicity parameter is known, which is not only convenient to measure but also independent of particle size. The hygroscopicity parameter of WSOM can be varied according to the choice of mixing components instead of by changing the algorithm itself. Similarly, some other water-soluble compo-

nents (e.g., sulfate) can be introduced into the inversion algorithm without laboratory measurements.

3.5 Uncertainty analysis

The uncertainty in the retrieval results was evaluated using synthetic data, both without and with input errors added. For the first case (without input errors), a set of complex refractive indices has been obtained by calculating a set of volume fractions of the aerosol components using the forward chemical model, which was used as input for the retrieval of the aerosol components without any noise added. For the aerosol components, the volume fraction of BC was constrained between 0.0 % to 3.0 % with an interval of 0.5 % and corresponding dynamic ranges for the other components with intervals of 10 %, in three ambient relative humidity conditions (40 %, 60 % and 80 %). Figure 5 shows the comparison of the aerosol component volume fractions from forward modeling used as input and their retrieved values. The volume fractions of the retrieved aerosol components reproduce the input values reasonably well. For the fine-mode fraction, most data pairs are located close to the 1 : 1 line, with a mean absolute error (MAE) of the aerosol component volume fractions of 3.0 %. In five samples the difference in the AW_f is more than 20.0 %, though the overall MAE for AW_f is only 5.5 %. In these five samples, the BC component is low and organic matter contributes substantially to the aerosol light absorption, resulting in underestimation of the AW_f volume fraction at high RH and overestimation for moderate RH. WSOM is overall slightly overestimated, and AN is underestimated by only a few percent. The correlation between the input and retrieved aerosol volume fractions in the coarse mode is even better than that in fine mode. The regression coefficient for all samples is 0.99, and the MAE is only 2.0 %. These results show the very small uncertainty in the retrieved aerosol component volume fractions.

To further evaluate the inversion results, errors were added to the synthetic data. To this end, three typical pollution cases were chosen in which the main pollutants are water-soluble aerosols, biomass burning aerosols and dust aerosols, respectively, hereafter referred to as WS, BB and DU pollution types. Each type is described by the different aerosol size distribution and refractive index parameters derived from Zhang et al. (2017). These parameters are listed in Table S1. Note that although the acronyms of the three pollution types are the same as the aerosol component names above, it does not mean that each type includes only one single aerosol component, as illustrated below.

Figure 6 shows the aerosol volume size distribution, complex refractive index and eight aerosol components in the WS, BB and DU types used in this exercise. For the size distribution, the highest volume concentrations occur in the fine mode of the WS and BB types, whereas for the DU type the coarse mode dominates. For the complex refractive index, significant absorption occurs in the fine-mode fraction of the

BB type, while relatively low absorption occurs in the other models. In the WS type, the mass fraction of AW_f is close to 20 % and for AN it is about 18 %, significantly larger than for the other types. By comparison, the BC mass fraction in the BB type is close to 3 %, and organic carbon is also high, with WSOM and WIOM mass fractions of 23 % and 11 %. In the DU type, the dust component is completely dominant, as expected, and the mass fractions of other components are less than 2 %.

The three main sources of error in the model input parameters are the RH and the complex refractive index in the fine and coarse modes. The uncertainties due to inversion errors in the modal refractive index were discussed in detail in Zhang et al. (2017) and are directly used here to estimate their effects on aerosol components. For RH, the observation error is about 5 % (WMO, 2008); in this exercise a larger error (10 %) is introduced to more rigorously assess the uncertainty in the estimated aerosol components. These typical uncertainties are listed in Table S2. The total relative error (TRE), which is the propagated relative error calculated by the mean aerosol component error induced by the errors in sub-CRIs and RH in three pollution types, is used to assess the uncertainty in the aerosol composition inversion. As shown in Table 3, the TRE of BC is 32.21 %, less than other components in the fine mode, and the largest source of TRE is the imaginary part of the complex refractive index ($k_f, 440$), with 25.68 %. Compared with BC, the TRE of OM is larger (about 75 %), primarily contributed to by RH, followed by n_f . The uncertainty in the imaginary part impacts very little due to the low absorption of OM. The uncertainty in AN due to the imaginary part is low, but a very high uncertainty is caused by RH. Another component of IS is SC which usually occurs in the coarse mode. The large TRE of SC is contributed to by the real part of the complex refractive index in the coarse mode (n_c), with 912.87 %, leading to the largest TRE of IS. Affected by SC, the TRE of AW_c is also large due to n_c , but the TRE of AW_f is much smaller (50.05 %). In the coarse mode, the TRE of DU is smallest in all of the aerosol components, only 15.79 %, mainly caused by n_c . Overall, most of the uncertainties in the fine mode are from RH, and those in the coarse mode are from n_c . Fortunately, the RH observed by ground-based stations is accurate, with an error which is usually less than about 5 % (WMO, 2008), which can significantly reduce the uncertainty in the retrieved aerosol scattering components. It should be noted that the uncertainties in Table 3 are for single measurements. One important advantage of remote sensing is that multiple measurements can be made during a short period of time. Thus, the average uncertainty in the aerosol components can be effectively reduced by taking into account independent errors in each observation. In addition, the accuracy of the retrieved n_c needs to be improved in order to deal with the aerosol component inversion.

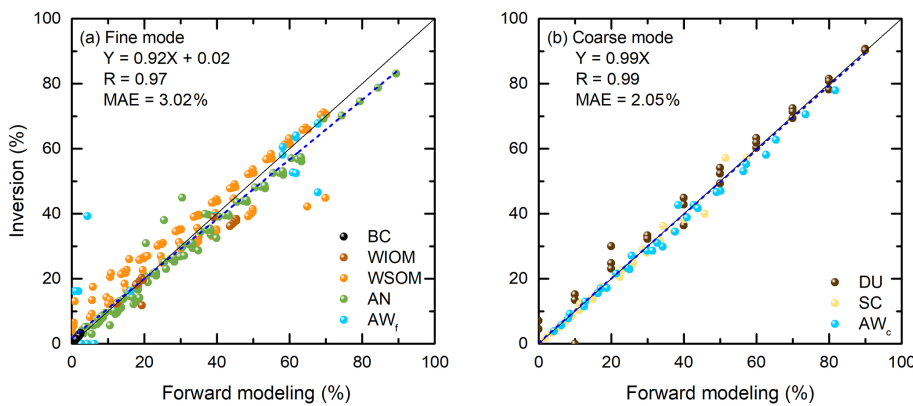


Figure 5. Scatterplots of volume fractions of aerosol components in the fine (**a**) and coarse (**b**) modes retrieved using the algorithm described in Sect. 3 versus those used as input calculated with the forward model. The solid line is the 1 : 1 line, and the dashed line is the fitting line.

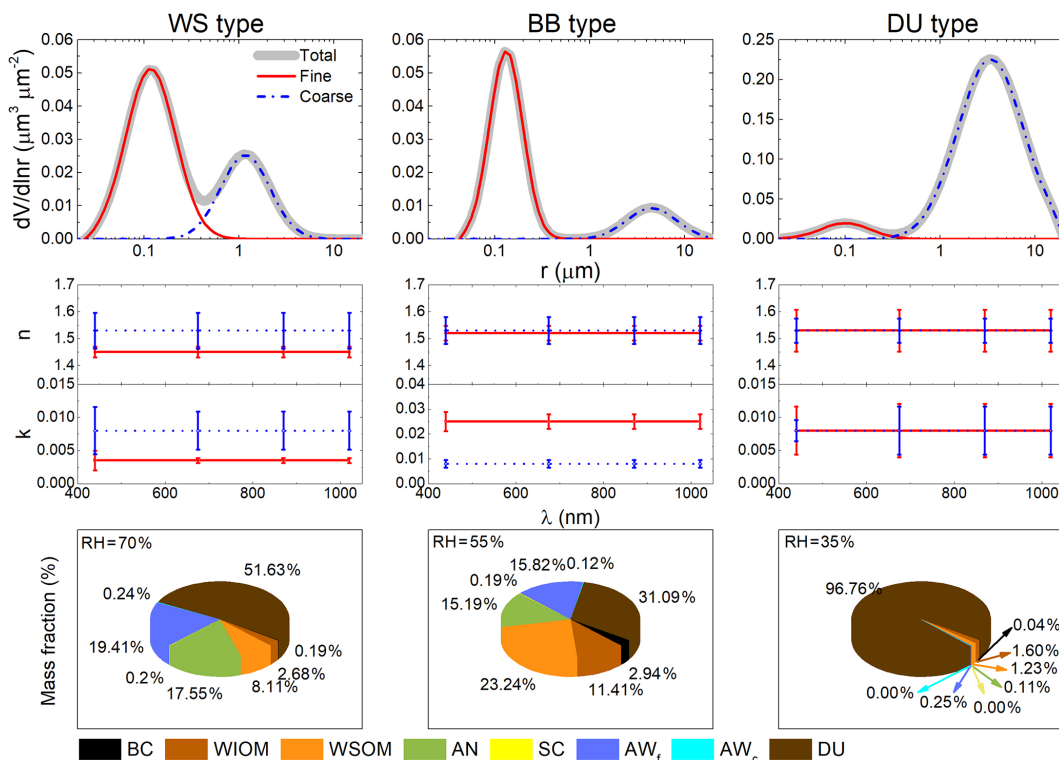


Figure 6. The fine- and coarse-mode volume size distribution, complex refractive index, and aerosol components describing the aerosol models used in the synthetic case study (WS: water soluble, BB: biomass burning, DU: dust).

4 Results

4.1 Aerosol component retrievals

The averaged mass fractions of the aerosol components measured at 16 SONET sites are presented in Fig. 7. Each pie chart is marked with the site name, coordinates, observation period and BC fraction. The mass fractions are also listed in Table S3. The pie charts show that the coarse-mode mass fraction usually dominates at the northern and northwestern

sites. The mass fraction of the dust component is significantly higher than that of others, with a fraction of more than 50 % at the western sites (Lhasa, Zhangye, Kashgar, Minqin and Xi'an) and the Beijing, Harbin and Songshan sites, which is different from surface observations of chemical components (Zhang et al., 2012; Liu et al., 2014). This is because sun photometers provide data integrated over the whole atmospheric column and thus include the dust transport layer near 4 km (Proestakis et al., 2018), where dust concentrations may be substantial, whereas surface observations are

Table 3. Estimated total relative errors (TREs) of aerosol component mass fractions in the three aerosol models used to evaluate the aerosol component classification inversion algorithm.

Aerosol		RH	Fine mode			Coarse mode			TRE*
components			n_f	$k_{f, 440}$	k_f	n_c	$k_{c, 440}$	k_c	
BC		5.74 %	0.59 %	25.68 %	18.57 %	0.00 %	0.00 %	0.00 %	32.21 %
OM	WIOM	75.82 %	4.55 %	5.28 %	1.08 %	0.00 %	0.00 %	0.00 %	76.15 %
	WSOM	51.60 %	51.92 %	3.44 %	2.11 %	0.00 %	0.00 %	0.00 %	73.31 %
IS	AN	207.00 %	60.86 %	7.07 %	6.04 %	0.00 %	0.00 %	0.00 %	215.96 %
	SC	25.71 %	0.00 %	0.00 %	0.00 %	912.51 %	2.16 %	1.23 %	912.87 %
AW	AW _f	49.77 %	3.80 %	3.71 %	0.00 %	0.00 %	0.00 %	0.00 %	50.05 %
	AW _c	8.95 %	0.00 %	0.00 %	0.00 %	912.55 %	2.10 %	1.17 %	912.60 %
DU		0.34 %	0.00 %	0.00 %	0.00 %	15.78 %	0.04 %	0.02 %	15.79 %

* TRE = $\sqrt{\sum_1^7 \bar{x}_i^2}$, where \bar{x} represents the mean error in aerosol components from three aerosol types. The RH is given input error of $\pm 10\%$, and the inversion errors in sub-CRIs are from Zhang et al. (2017) listed in Table S2.

local point measurements. The lowest dust fractions are observed at southern sites, especially at the Guangzhou site, with a mass fraction of 31.5 %. In contrast, the water content is dominant at southern sites in both the fine and coarse modes. The maximum AW (AW_f and AW_c) fraction occurs at the Guangzhou site (28.7 %), and the lowest mass fractions of 2.0 % and 7.5 % are observed at the Lhasa and Kashgar sites, respectively. High AW_f occurs in the cities of east central China due to the higher occurrence of inorganic salts with larger hygroscopicity in the fine mode at these sites, whereas the dominant AW_c in the western sites can be explained by the inorganic salt coating of larger particles in the dust source region (Rosenfeld et al., 2001). The IS fraction (AN and SC) gradually increases from north to south, which is consistent with the trend of the water content. The fraction of the AN subcomponent is less than 7.0 % at Lhasa, Zhangye, Kashgar and Minqin, whereas it is more than 20 % at Chengdu, Guangzhou, Haikou and Sanya. At the Zhoushan site a high AN fraction is also observed, up to 17.1 %. For the SC component, the maximum value occurs at the Kashgar (17.1 %) site. The high SC fraction at the southeast coastal sites is readily ascribed to the influence of the ocean; the high SC fraction at the Kashgar site is due to the paleomarine source of dust over the Taklamakan Desert (Huang et al., 2010). The WIOM component fraction is high in the central sites but relatively low in the southern coastal and northwest sites. For the WSOM component, the low value of less than 3 % appears only at northwestern sites (Zhangye, Kashgar and Minqin). In the atmospheric column, the mass fraction of the BC component averaged over 16 sites is only 0.59 %, lower than from near-surface in situ observations (usually 1 %–5 %), which implies that the BC fraction may be reduced by the suspended layer with other components such as dust aerosols. Nevertheless, the unusually high mass fraction of BC in Shanghai could be due to observation uncertainty, also

accompanied by the large error for aerosol component inversion.

The closure of the CRI between instantaneous optical–physical inversion and chemical estimation is examined by the data pair frequency. Figure 8 shows scatter density plots of the chemically estimated and sun-photometer-retrieved imaginary parts of the fine mode at 675 nm (k_f) and 440 nm ($k_{f, 440}$) and the real parts of the fine mode at 440 nm (n_f). The points are colored by the number of data pairs (retrieved, estimated), which are sorted according to ordered pairs in 0.0005 intervals for the imaginary parts of the CRI and 0.001 intervals for the real parts. The data pairs of k_f are closely concentrated around the 1 : 1 line, although a slight underestimation is observed with 94.3 % of the estimated values lower than the retrieved values; only 5.3 % of the data pairs have a relatively large absolute error (AE > 0.01). The mean bias is not large (-0.003), and the mean absolute value is equal to the mean absolute error (MAE = 0.003). There are two reasons for this slight underestimation in chemical estimation. On the one hand, the imaginary part of the refractive index of BC is much larger than for the other components due to its strong absorption. Thus, the inversion of the BC concentration is very sensitive to the estimation of the refractive index. As shown in Table 3, although the TRE of BC is the lowest, the errors caused by k_f and $k_{f, 440}$ are larger than for any other component. On the other hand, k_f is not only affected by BC in the inversion process but also affected by organic components (WSOM and WIOM) with spectral absorption characteristics. Therefore, in most cases, k_f is underestimated in chemical estimation and $k_{f, 440}$ is overestimated (bias = 0.007). The mean relative error (RE) is 27.1 %, and 62.8 % of the data points are below the average relative error line. This indicates that most inversion results have good optical closure. For the closure of the real part of the fine mode, the data pairs of n_f are also concentrated around the

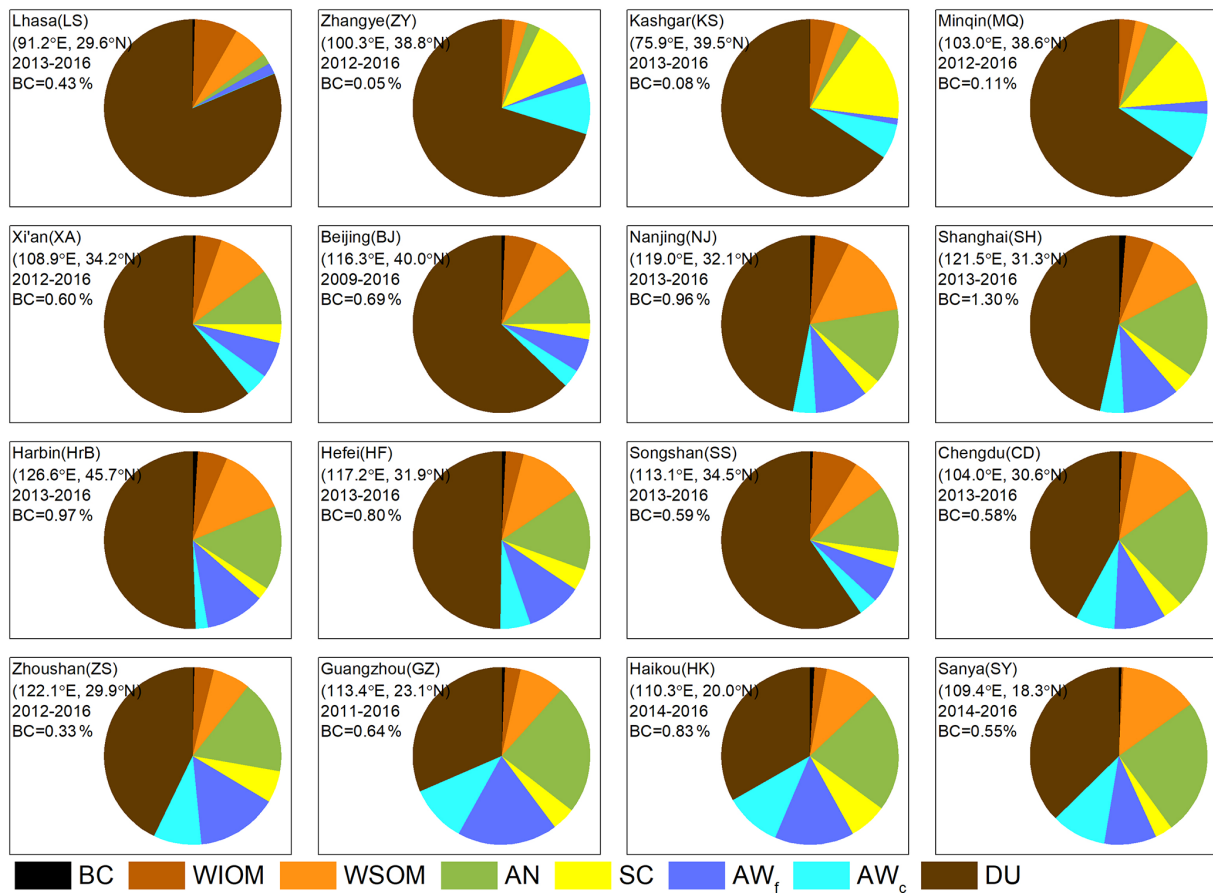


Figure 7. The averaged mass fraction of aerosol components at SONET sites. The site name, location, observation period and BC fraction are marked in each subgraph. The mass fractions of other components are listed in Table S3.

identity line, although 76.5 % of the n_f is above the identity line. Underestimation occurs mainly when n_f is larger than 1.56, because the only component with the real part of the CRI larger than 1.56 is BC, but its concentration is mainly determined by the imaginary part. The bias of the estimated n_f (bias = 0.009) is larger than that of k_f due to the fact that the value and the range of n_f are larger than those of k_f .

In addition, the comparison of aerosol components with those from Zhang et al. (2018) is given in Sect. S3. Figures S1 and S2 demonstrate that the algorithm in this study shows a positive effect on AN and AW_f, although there are few validation points.

4.2 Seasonal variation

The seasonal variation in the aerosol component mass concentrations, averaged over 15 stations (Lhasa is not used due to lack of adequate seasonal data) and all available years, is shown as box-and-whisker plots in Fig. 9. The top and bottom edges of each box represent the top and bottom quartiles (Q3 and Q1), and the corresponding whiskers are the outliers ($Q3 + 1.5 \text{IQR}$ and $Q1 - 1.5 \text{IQR}$; IQR is interquar-

tile range). The mean value is indicated by a plus sign (+), and the median value is indicated by a short line inside the box (—). Figure 9 shows that the DU component exhibits an obvious seasonality. The DU mass concentration is very high in the spring, and the mean value reaches up to 332.9 mg m^{-3} due to dust transport from the northwest of China. With the weakening of dust transport and the increase in moisture, the DU fraction decreases in other seasons, with a mean value of around 240.0 mg m^{-3} . Although the DU concentration is lower in the summer than in other seasons, it is still relatively high near the dust source area, which results in a large difference between the upper and lower quartiles. In contrast, the AN mass concentration mean value peaks in the summer (76.8 mg m^{-3}), whereas a minimum occurs in the spring (47.7 mg m^{-3}). It is worth noting that although the mean value in the winter is not high (51.1 mg m^{-3}), the interval between the upper and lower quartiles of AN is the smallest in the winter. The minimum value of AN (17.9 mg m^{-3}) is higher than in other seasons (4.1 mg m^{-3} in spring, 9.5 mg m^{-3} in summer and 11.1 mg m^{-3} in autumn). The seasonal variation in the water content is slightly different from that of inorganic salts. The low values of mean AW_f

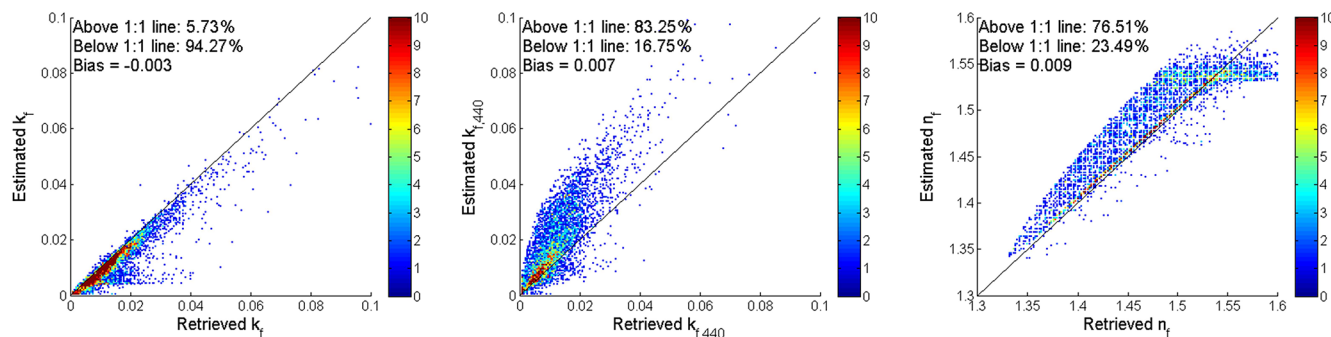


Figure 8. Data pair frequency of instantaneous imaginary parts of the complex refractive index at 675 nm (k_f) and 440 nm ($k_{f,440}$) and the real part at 440 nm (n_f) which are sorted according to ordered pairs (retrieved, estimated) in 0.0005 and 0.001 intervals for imaginary and real parts, respectively. “Retrieved” represents the subcomponent of the CRI from the optical–physical retrievals, and “estimated” is estimated by retrieved chemical components. The color represents the number of cases (color bar), and the solid black line shows the 1 : 1 line.

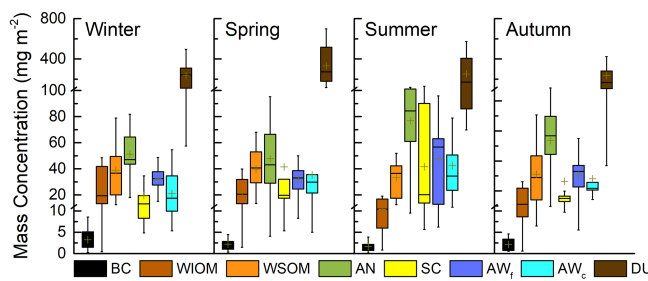


Figure 9. The mass concentrations of aerosol components in four seasons (winter, spring, summer and autumn). For the box-and-whisker plot, the mean value is indicated by a plus sign (+), and the median value is indicated by a short line inside the box (—). The top and bottom edges of each box represent the top and bottom quartiles (Q3 and Q1), and the corresponding whiskers are the outliers ($Q3 + 1.5\text{IQR}$ and $Q1 - 1.5\text{IQR}$; IQR is interquartile range).

occur in the spring, while AW_c is significantly lower in the winter (21.0 mg m^{-2}) than in other seasons. The difference between the upper and lower quartiles of AW_f in the summer is larger than in other seasons, indicating that in the summer the aerosol at some sites has a low hygroscopicity. The OM mass concentration is slightly higher in the winter than that in other seasons probably due to the occurrence of haze pollution in the winter, with mean concentrations of the WIOM and WSOM fractions of 22.3 and 38.8 mg m^{-2} , respectively. In the summer, the OM concentration is only about two-thirds of that in the winter. The median value of the BC mass concentration is higher in the winter (3.0 mg m^{-2}), which can be related to heating in northern China. Low concentrations of BC in the other seasons are mainly due to the influence of frequent dust events in the spring and high aerosol hygroscopic growth in the summer. Similarly to AN, the SC concentration peaks in the summer and has a minimum in the winter, due to the influence of the Asian monsoon. The median values in these two seasons are 41.6 and 19.6 mg m^{-2} , respectively.

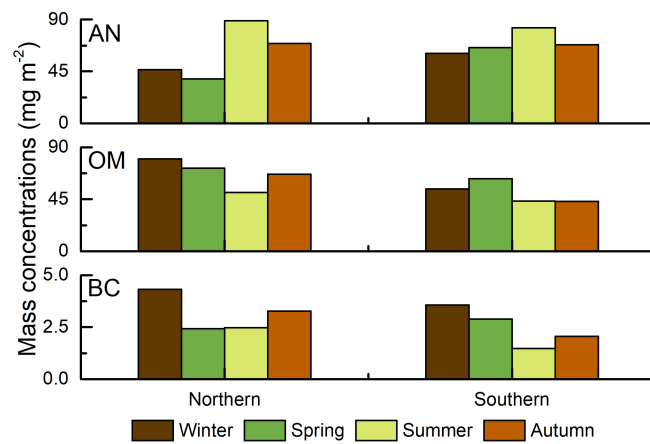


Figure 10. Comparison of aerosol component mass concentrations in northern (Xi'an, Beijing, Harbin, Hefei and Songshan) and southern (Nanjing, Shanghai, Zhoushan, Guangzhou, Haikou and Sanya) China.

The seasonal variation in the main aerosol components in the fine mode is discussed on a regional basis (Fig. 10). BC concentrations in typical northern regions are higher than in southern regions, because of emissions due to winter heating only in the north. Other BC sources are vehicle emissions and biomass burning. Adverse meteorological conditions in winter result in the accumulation of BC in the atmosphere resulting in high BC values in both the north and the south. The highest BC mass concentration in the northern region in the winter is 4.3 mg m^{-2} . OM is one of the dominant components in the fine mode, with sources similar to those of BC. The impact of biomass burning in the winter and spring over southern China (Chen et al., 2017) is significant, leading to OM concentrations of more than 50.0 mg m^{-2} . In the northern region, much biomass burning occurs in the autumn (Wang et al., 2020). With the influence of heating, the OM level in the north can reach up to 80.1 mg m^{-2} . Therefore, the OM mass concentration in the northern region is only low

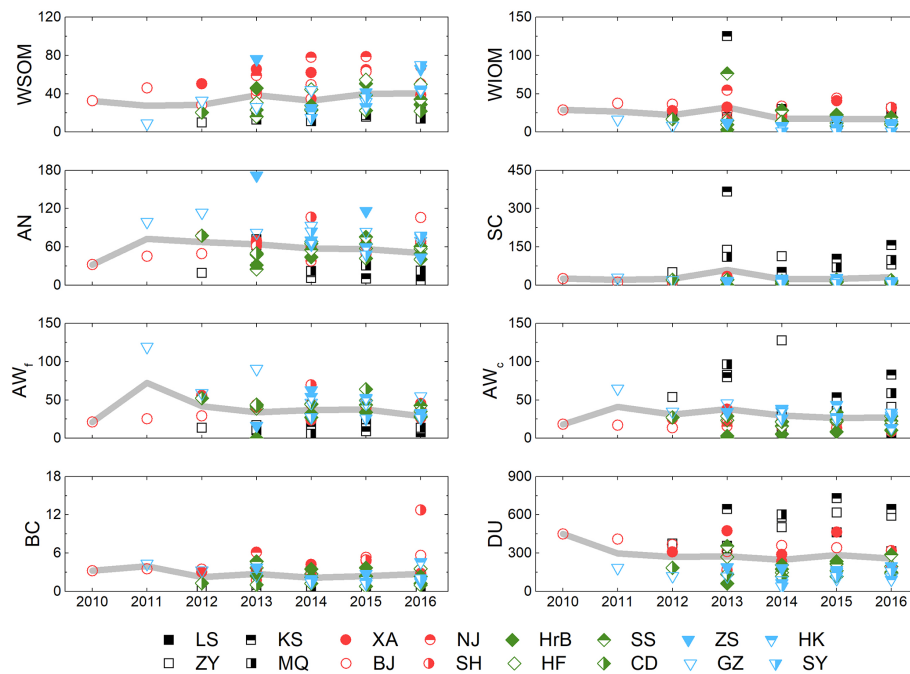


Figure 11. The interannual variations in mean aerosol component mass concentrations integrated over the whole atmospheric column with SONET sites from 2010 to 2016. The gray line represents the mean mass concentration of aerosol components averaged over the 16 sites; the points in each graph show the yearly value at each site. The abbreviations for the site names are from Table 1.

in the summer (50.8 mg m^{-2}). AN is usually formed by secondary reactions of gaseous precursors in complex air pollution areas. In both the northern and the southern region, AN mass concentration is larger in the summer than in other seasons, and the seasonal variation in the southern region is significantly smaller than that in the north. The mean AN mass concentration in the southern region is 8.7 mg m^{-2} higher than that in the northern region. This suggests that more AN is produced by secondary reactions in the humid climate in the south than in the northern region.

4.3 Interannual variation

Figure 11 shows the interannual variations in the aerosol component mass concentrations in the atmospheric column from 2010 to 2016. The 16 SONET sites have been established in succession, so the number of available observations increased year by year with the longest time series from the Beijing site (see also Table 1). The annual mean mass concentrations shown in Fig. 11 are averages over all sites; i.e., the number of sites was not accounted for, and, in particular in the earlier years (2010–2011), the annual mean may thus be representative of one (Beijing) or a few sites. Therefore, the annual means for each site available have been plotted as well. Figure 11 shows that the annual mean mass concentrations of most of the aerosol components in the fine mode increased in most of the first years and then decreased. Influenced by China's environmental control policies, the mean AN decreased significantly from

72.4 mg m^{-2} in 2011 to 50.5 mg m^{-2} in 2016, i.e., a reduction by 21.9 mg m^{-2} . The yearly mass concentrations of AN at most sites also follow a downward trend, and AN in the southeastern coastal sites is significantly higher than that in the northwestern sites. In contrast, the mean BC mass concentration shows a peak (3.9 mg m^{-2}) in 2011, drops in 2012 to the lowest value during the whole period (2.3 mg m^{-2}) and then increases somewhat to a second peak (2.7 mg m^{-2}) in 2013. After a decrease in 2014, BC climbed to 2.8 mg m^{-2} in 2016. In the southeastern coastal and northwestern sites, BC concentrations were relatively low. The unusually high values at Shanghai in 2016 may be due to observational errors. Similarly to BC, AW_f also experienced a small fluctuation after a significant decline in 2012. The AW_f in aerosol measured at the southern sites is higher than that at other sites. The fine-mode WIOM and WSOM components show different behavior. WIOM reached a peak in 2013, with the peak value of 32.3 mg m^{-2} , and then showed a significant decline after 2013. WSOM also reached a peak concentration of 35.8 mg m^{-2} in 2013, which is 2 mg m^{-2} lower than the peak in 2016, and overall the concentrations increased. These results suggest that the policy of air pollution control in China is effective in controlling inorganic salts and WIOM aerosols, while WSOM still needs to be further controlled. The concentrations of the coarse-mode aerosol components fluctuate somewhat during the observation period, with a slight peak in 2013. The concentration of each component in the coarse mode at the northwestern sites is higher than those at other

sites, which can be related to the high fraction of large particles. Due to the large influence of geographical factors on the coarse-mode aerosol components, DU in 2010 (only Beijing site) was significantly larger than in other years. Since 2014, the mean DU mass concentration has increased, while a downward tendency has been observed in the AW_c and SC concentrations since 2013. Coarse-mode aerosols usually derive from natural sources, and their variations can be associated with changes in the meteorological conditions.

5 Conclusions and discussions

The accurate measurement of atmospheric aerosol components plays an important role in reducing uncertainty in climate assessment. In the current study, we updated the refractive index calculation in a multicomponent liquid system and improved the component inversion algorithm of Zhang et al. (2018) to retrieve atmospheric columnar aerosol components including black carbon (BC), organic matter (WSOM and WIOM), inorganic salt (AN and SC), dust-like content (DU), and water content in the fine and coarse modes (AW_f and AW_c). This algorithm was applied to data from the SONET sun photometer network, and the regional distribution and interannual variation in atmospheric aerosol components in China were analyzed for the period from 2010 to 2016. The results show that the dust-like component is dominant in northern China but the aerosol water content (AW_f and AW_c) is dominant in the southern coastal region. The inorganic salt (AN) in the fine mode has a significant seasonal variation, with a mass concentration of 76.8 mg m⁻² in the summer which is significantly higher than that in other seasons. Meanwhile, the AN concentrations have significantly decreased from 2011 to 2016, which is inseparable from China's environmental control policies. However, the slight increase in WSOM and BC is still noteworthy.

As the aerosol concentrations in the atmospheric column obtained from the inversion of remote sensing data are different from those measured by in situ measurements near the surface, such as with on-line aerosol mass spectrometers, the validation of the retrieval results is difficult. Proestakis et al. (2018) used data from the Cloud-Aerosol Lidar with Orthogonal Polarization (CALIOP) on the CALIPSO satellite to analyze the distribution of mineral dust over China, and the results show a higher concentration of the DU component in the atmospheric column over northern China. Similarly, Huang et al. (2010) provided a basis for the high SC content at the Kashgar station due to the paleomarine source. However, for the direct comparison of our retrievals with independent data, airborne measurements of the vertical distribution of atmospheric aerosol components are needed (Kahn et al., 2017). In future research, we will design a verification experiment to comprehensively evaluate the results from our inversion method.

The method presented can be used not only for ground-based sun-sky photometer measurements but also for other remote sensing instruments (e.g. lidar) and even for satellite remote sensing in the future. Meanwhile, as long as measurements of multiwavelength extinction coefficients and aerosol particle size distributions are available, the inversion of atmospheric particulate matter composition can also be performed using comprehensive observations with multiple instruments near the surface. Therefore, this method can be widely used in low-cost and wide-area measurements in the future, providing a possibility for obtaining the global distribution of aerosol composition.

Data availability. The aerosol component data used in this study can be requested from the corresponding author (lizq@radi.ac.cn).

Supplement. The supplement related to this article is available online at: <https://doi.org/10.5194/acp-20-12795-2020-supplement>.

Author contributions. ZL conceived and designed the study. YC collected and processed the meteorological data. KL and YX collected the remote sensing data. CZ collected the DEM data and drew the map. YZ improved the aerosol component method and performed the inversions. YZ analyzed the spatiotemporal trends of aerosol component concentrations. YZ and GL prepared the paper with contributions from all coauthors.

Competing interests. The authors declare that they have no conflict of interest.

Special issue statement. This article is part of the special issue “Satellite and ground-based remote sensing of aerosol optical, physical, and chemical properties over China”. It is not associated with a conference.

Acknowledgements. This work was supported by the National Natural Science Foundation of China (41925019, 41601386) and the National Key R&D Program of China (2016YFE0201400).

Financial support. This work was supported by the National Natural Science Foundation of China (grant nos. 41925019 and 41601386) and the National Key R&D Program of China (grant no. 2016YFE0201400).

Review statement. This paper was edited by Stelios Kazadzis and reviewed by three anonymous referees.

References

- Arola, A., Schuster, G., Myhre, G., Kazadzis, S., Dey, S., and Tripathi, S. N.: Inferring absorbing organic carbon content from AERONET data, *Atmos. Chem. Phys.*, 11, 215–225, <https://doi.org/10.5194/acp-11-215-2011>, 2011.
- Bond, T. and Bergstrom, R.: Light absorption by carbonaceous particles: an investigative review, *Aerosol. Sci. Tech.*, 40, 27–67, 2006.
- Boucher, O., Randall, D., Artaxo, P., Bretherton, C., Feingold, G., Forster, P., Kärninen, V.-M., Kondo, Y., Liao, H., Lohmann, U., Rasch, P., Satheesh, S. K., Sherwood, S., Stevens, B., and Zhang, X. Y.: Clouds and Aerosols, in: Climate Change 2013: The Physical Science Basis. Contribution of Working Group I to the Fifth Assessment Report of the Intergovernmental Panel on Climate Change, edited by: Stocker, T. F., Qin, D., Plattner, G.-K., Tignor, M., Allen, S. K., Boschung, J., Nauels, A., Xia, Y., Bex, V., and Midgley, P. M., Cambridge University Press, Cambridge, United Kingdom and New York, NY, USA, 2013.
- Bougiatioti, A., Zarmpas, P., Koulouri, E., Antoniou, M., Theodosi, C., Kouvarakis, G., Saarikoski, S., Mäkelä, T., Hillamo, R., and Mihalopoulos, N.: Organic, elemental and water-soluble organic carbon in size segregated aerosols, in the marine boundary layer of the Eastern Mediterranean, *Atmos. Environ.*, 64, 251–262, 2013.
- Chalbot, M. G., Chitranshi, P., da Costa, G. G., Pollock, E., and Kavouras, I. G.: Characterization of water-soluble organic matter in urban aerosol by ^1H -NMR spectroscopy, *Atmos. Environ.*, 128, 235–245, 2016.
- Chen, J., Li, C., Ristovski, Z., Milic, A., Gu, Y., Islam, M., Wang, S., Hao, J., Zhang, H., He, C., Guo, H., Fu, H., Miljevic, B., Morawska, L., Thai, P., Lam, Y., Pereira, G., Ding, A., Huang, X., and Dumka, U. C.: A review of biomass burning: Emissions and impacts on air quality, health and climate in China, *Sci. Total Environ.*, 579, 1000–1034, 2017.
- Chen, Y. and Bond, T. C.: Light absorption by organic carbon from wood combustion, *Atmos. Chem. Phys.*, 10, 1773–1787, <https://doi.org/10.5194/acp-10-1773-2010>, 2010.
- Choi, Y. and Ghim, Y. S.: Estimation of columnar concentrations of absorbing and scattering fine mode aerosol components using AERONET data, *J. Geophys. Res.-Atmos.*, 121, 13628–13640, 2016.
- Drozd, G., Woo, J., Häkkinen, S. A. K., Nenes, A., and McNeill, V. F.: Inorganic salts interact with oxalic acid in submicron particles to form material with low hygroscopicity and volatility, *Atmos. Chem. Phys.*, 14, 5205–5215, <https://doi.org/10.5194/acp-14-5205-2014>, 2014.
- Dubovik, O. and King, M.: A flexible inversion algorithm for retrieval of aerosol optical properties from sun and sky radiance measurements, *J. Geophys. Res.-Atmos.*, 105, 20 673–20 696, 2000.
- Dubovik, O., Smirnov, A., Holben, B. N., King, M. D., Kaufman, Y. J., Eck, T. F., and Slutsker, I.: Accuracy assessments of aerosol optical properties retrieved from aerosol robotic network (AERONET) Sun and sky radiance measurements, *J. Geophys. Res.-Atmos.*, 105, 9791–9806, 2000.
- Dubovik, O., Herman, M., Holdak, A., Lapyonok, T., Tanré, D., Deuzé, J. L., Ducos, F., Sinyuk, A., and Lopatin, A.: Statistically optimized inversion algorithm for enhanced retrieval of aerosol properties from spectral multi-angle polarimetric satellite observations, *Atmos. Meas. Tech.*, 4, 975–1018, <https://doi.org/10.5194/amt-4-975-2011>, 2011.
- Ganguly, D., Ginoux, P., Ramaswamy, V., Dubovik, O., Welton, J., Reid, E. A., and Holben, B. N.: Inferring the composition and concentration of aerosols by combining AERONET and MPLNET data: Comparison with other measurements and utilization to evaluate GCM output, *J. Geophys. Res.-Atmos.*, 114, D16203, <https://doi.org/10.1029/2009JD011895>, 2009.
- Heller, W.: Remarks on refractive index mixture rules, *J. Phys. Chem.*, 69, 1123–1129, 1965.
- Huang, K., Zhuang, G., Li, J., Wang, Q., Sun, Y., Lin, Y., and Fu, J. S.: Mixing of Asian dust with pollution aerosol and the transformation of aerosol components during the dust storm over China in spring 2007, *J. Geophys. Res.*, 115, D00K13, <https://doi.org/10.1029/2009JD013145>, 2010.
- Jing, B., Tong, S., Liu, Q., Li, K., Wang, W., Zhang, Y., and Ge, M.: Hygroscopic behavior of multicomponent organic aerosols and their internal mixtures with ammonium sulfate, *Atmos. Chem. Phys.*, 16, 4101–4118, <https://doi.org/10.5194/acp-16-4101-2016>, 2016.
- Kahn, R. A., Berkoff, T. A., Brock, C., Chen, G., Ferrare, R. A., Ghan, S., Hansico, T. F., Hegg, D. A., Vanderlei Martins, J., McNaughton, C. S., Murphy, D. M., Ogren, J. A., Penner, J. E., Pilewskie, P., Seinfeld, J. H., and Worsnop, D. R.: SAM-CAAM: A Concept for Acquiring Systematic Aircraft Measurements to Characterize Aerosol Air Masse, *B. Am. Meteorol. Soc.*, 98, 2215–2228, <https://doi.org/10.1175/BAMS-D-16-0003.2>, 2017.
- Kandler, K. and Schütz, L.: Climatology of the average water-soluble volume fraction of atmospheric aerosol, *Atmos. Res.*, 83, 77–92, 2007.
- Kreidenweis S. M., Petters, M. D., and DeMott, P.: Single-parameter estimates of aerosol water content, *Environ. Res. Lett.*, 3, 035002, <https://doi.org/10.1088/1748-9326/3/3/035002>, 2008.
- Krivácsy, Z., Gelencsér, A., Kiss, G., Mészáros, E., Molnár, Á., Hoffer, A., Mészáros, T., Sárvári, Z., Temesi, D., Varga, B., Baltensperger, U., Nyeki, S., and Weingartner, E.: Study on the chemical character of water soluble organic compounds in fine atmospheric aerosol at the jungfraujoch, *J. Atmos. Chem.*, 39, 235–259, 2001.
- Koven, C. and Fung, I.: Inferring dust composition from wavelength-dependent absorption in Aerosol Robotic Network AERONET data, *J. Geophys. Res.*, 111, D14205, <https://doi.org/10.1029/2005JD006678>, 2006.
- Lesins, G., Chylek, P., and Lohmann, U.: A study of internal and external mixing scenarios and its effect on aerosol optical properties and direct radiative forcing, *J. Geophys. Res.-Atmos.*, 107, 4094, <https://doi.org/10.1029/2001JD000973>, 2002.
- Li, L., Dubovik, O., Derimian, Y., Schuster, G. L., Lapyonok, T., Litvinov, P., Ducos, F., Fuertes, D., Chen, C., Li, Z., Lopatin, A., Torres, B., and Che, H.: Retrieval of aerosol components directly from satellite and ground-based measurements, *Atmos. Chem. Phys.*, 19, 13409–13443, <https://doi.org/10.5194/acp-19-13409-2019>, 2019.
- Li, Z., Gu, X., Wang, L., Li, D., Xie, Y., Li, K., Dubovik, O., Schuster, G., Goloub, P., Zhang, Y., Li, L., Ma, Y., and Xu, H.: Aerosol physical and chemical properties retrieved from ground-based remote sensing measurements during heavy haze days in Beijing winter, *Atmos. Chem. Phys.*, 13, 10171–10183, <https://doi.org/10.5194/acp-13-10171-2013>, 2013.

- Li, Z., Xu, H., Li, K. T., Li, D. H., Xie, Y. S., Li, L., Zhang, Y., Gu, X. F., Zhao, W., Tian, Q. J., Deng, R. R., Su, X. L., Qiao, Y. L., Cui, W. Y., Hu, Y., Gong, C. L., Wang, Y. Q., Wang, X. F., Wang, J. P., Du, W. B., Pan, Z. Q., Li, Z. Z., and Bu, D.: Comprehensive study of optical, physical, chemical, and radiative properties of total columnar atmospheric aerosols over China: An overview of Sun-Sky Radiometer Observation Network (SONET) measurements, *B. Am. Meteorol. Soc.*, 99, 739–755, 2018.
- Li, Z., Zhang, Y., Xu, H., Li, K., Dubovik, O., and Goloub, P.: The fundamental aerosol models over China region: A cluster analysis of the ground-based remote sensing measurements of total columnar atmosphere, *Geophys. Res. Lett.*, 46, 4924–4932, <https://doi.org/10.1029/2019GL082056>, 2019.
- Liu, Q., Liu, Y., Yin, J., Zhang, M., and Zhang, T.: Chemical characteristics and source apportionment of PM₁₀ during Asian dust storm and non-dust storm days in Beijing, *Atmos. Environ.*, 91, 85–94, 2014.
- Ma, Q., He, H., and Liu, C.: Hygroscopic properties of oxalic acid and atmospherically relevant oxalates, *Atmos. Environ.*, 69, 281–288, 2013.
- Mayol-Bracero, O. L., Guyon, P., Graham, B., Roberts, G., Andreae, M. O., Decesari, S., Facchini, M. C., Fuzzi, S., and Artaxo, P.: Water-soluble organic compounds in biomass burning aerosols over Amazonia 2. apportionment of the chemical composition and importance of the polyacidic fraction, *J. Geophys. Res.*, 107, 8091, <https://doi.org/10.1029/2001JD000336>, 2002.
- McConnell, C. L., Highwood, E. J., Coe, H., Formenti, P., Anderson, B., Osborne, S., Nava, S., Desboeufs, K., Chen, G., and Harrison, M. A. J.: Seasonal variations of the physical and optical characteristics of Saharan dust: Results from the Dust Outflow and Deposition to the Ocean (DODO) experiment, *J. Geophys. Res.-Atmos.*, 113, D14S05, <https://doi.org/10.1029/2007JD009606>, 2008.
- Petters, M. D. and Kreidenweis, S. M.: A single parameter representation of hygroscopic growth and cloud condensation nucleus activity, *Atmos. Chem. Phys.*, 7, 1961–1971, <https://doi.org/10.5194/acp-7-1961-2007>, 2007.
- Proestakis, E., Amiridis, V., Marinou, E., Georgoulas, A. K., Solomos, S., Kazadzis, S., Chimot, J., Che, H., Alexandri, G., Bini etoglou, I., Daskalopoulou, V., Kourtidis, K. A., de Leeuw, G., and van der A, R. J.: Nine-year spatial and temporal evolution of desert dust aerosols over South and East Asia as revealed by CALIOP, *Atmos. Chem. Phys.*, 18, 1337–1362, <https://doi.org/10.5194/acp-18-1337-2018>, 2018.
- Rosenfeld, D., Rudich, Y., and Lahav, R.: Desert dust suppressing precipitation: a possible desertification feedback loop, *P. Natl. Acad. Sci. USA*, 98, 5975–5980, 2001.
- Satheesh, S. K. and Krishna, M. K.: Radiative effects of natural aerosols: A review, *Atmos. Environ.*, 39, 2089–2110, 2005.
- Satheesh, S. K. and Srinivasan, J.: Enhanced aerosol loading over Arabian Sea during the pre-monsoon season: Natural or anthropogenic, *Geophys. Res. Lett.*, 29, 211–214, 2002.
- Satheesh, S. K., Ramanathan, V., Li-Jones, X., Lobert, J. M., Podgorny, I. A., Prospero, J. M., Holben, B. N., and Loeb, N. G.: A model for the natural and anthropogenic aerosols over the tropical Indian Ocean derived from Indian Ocean Experiment data, *J. Geophys. Res.*, 104, 27421–27440, 1999.
- Satheesh, S. K., Ramanathan, V., Holben, B. N., Moorthy, K. K., Loeb, N. G., Maring, H., Prospero, J. M., and Savoie, D.: Chemical, microphysical, and radiative effects of Indian Ocean aerosols, *J. Geophys. Res.*, 107, 4725, <https://doi.org/10.1029/2002JD002463>, 2002.
- Schuster, G. L., Lin, B., and Dubovik, O.: Remote sensing of aerosol water uptake, *Geophys. Res. Lett.*, 36, L03814, <https://doi.org/10.1029/2008GL036576>, 2009.
- Schuster, G. L., Dubovik, O., Holben, B. N., and Clothiaux, E. E.: Inferring black carbon content and specific absorption from Aerosol Robotic Network (AERONET) aerosol retrievals, *J. Geophys. Res.*, 110, D10S17, <https://doi.org/10.1029/2004JD004548>, 2005.
- Schuster, G. L., Dubovik, O., and Arola, A.: Remote sensing of soot carbon – Part 1: Distinguishing different absorbing aerosol species, *Atmos. Chem. Phys.*, 16, 1565–1585, <https://doi.org/10.5194/acp-16-1565-2016>, 2016.
- Sun, H., Biedermann, L., and Bond, T.: Color of brown carbon: a model for ultraviolet 20 and visible light absorption by organic carbon aerosol, *Geophys. Res. Lett.*, 34, L17813, <https://doi.org/10.1029/2007GL029797>, 2007.
- Tang, I. N.: Chemical and size effects of hygroscopic aerosol on light scattering coefficients, *J. Geophys. Res.*, 101, 19245–19250, 1996.
- Toon, O. B., Pollack, J. B., and Khare, B. N.: The optical constants of several atmospheric aerosol species: Ammonium sulfate, aluminum oxide, and sodium chloride, *J. Geophys. Res.*, 81, 5733–5748, 1976.
- van Beelen, A. J., Roelofs, G. J. H., Hasekamp, O. P., Henzing, J. S., and Röckmann, T.: Estimation of aerosol water and chemical composition from AERONET Sun-sky radiometer measurements at Cabauw, the Netherlands, *Atmos. Chem. Phys.*, 14, 5969–5987, <https://doi.org/10.5194/acp-14-5969-2014>, 2014.
- Wagner, R., Ajtai, T., Kandler, K., Lieke, K., Linke, C., Müller, T., Schnaiter, M., and Vragel, M.: Complex refractive indices of Saharan dust samples at visible and near UV wavelengths: a laboratory study, *Atmos. Chem. Phys.*, 12, 2491–2512, <https://doi.org/10.5194/acp-12-2491-2012>, 2012.
- Wang, L., Li, Z. Q., Tian, Q. J., Ma, Y., Zhang, F. X., Zhang, Y., Li, D. H., Li, K. T., and Li, L.: Estimate of aerosol absorbing components of black carbon, brown carbon, and dust from ground-based remote sensing data of sun-sky radiometers, *J. Geophys. Res.*, 118, 6534–6543, 2013.
- Wang, L., Jin, X., Wang, Q., Mao, H., Liu, Q., Weng, G., and Wang, Y.: Spatial and temporal variability of open biomass burning in Northeast China from 2003 to 2017, *Atmos. Ocean. Sci. Lett.*, 13, 240–247, <https://doi.org/10.1080/16742834.2020.1742574>, 2020.
- Wozniak, A. S., Shelley, R. U., Sleighter, R. L., Abdulla, H. A. N., Morton, P. L., Landing, W. M., and Hatcher, P. G.: Relationships among aerosol water soluble organic matter, iron and aluminum in European, North African, and Marine air masses from the 2010 US GEOTRACES cruise, *Mar. Chem.*, 154, 24–33, 2013.
- WMO: Guide to Meteorological Instruments and Methods of Observation, seventh edn. (WMO No.8), World Meteorological Organization, Geneva, Switzerland, 2008.
- Xie, Y., Li, Z., Zhang, Y. X., Zhang, Y., Li, D. H., Li, K. T., Xu, H., Zhang, Y., Wang, Y. Q., Chen, X. F., Schauer, J. J., and Bergin, M.: Estimation of atmospheric aerosol composition from ground-based remote sensing measurements of

- Sun-sky radiometer, *J. Geophys. Res.-Atmos.*, 122, 498–518, <https://doi.org/10.1002/2016JD025839>, 2017.
- Zappoli, S., Andracchio, A., Fuzzi, S., Facchini, M. C., Gelencsér, A., Kiss, G., Krivácsy, Z., Molnár, Á., Mészáros, E., Hansson, H.-C., Rosman, K., and Zebühr, Y.: Inorganic, organic and macromolecular components of fine aerosol in different areas of Europe in relation to their water solubility, *Atmos. Environ.*, 33, 2733–2743, 1999.
- Zhang, X. Y., Wang, Y. Q., Niu, T., Zhang, X. C., Gong, S. L., Zhang, Y. M., and Sun, J. Y.: Atmospheric aerosol compositions in China: spatial/temporal variability, chemical signature, regional haze distribution and comparisons with global aerosols, *Atmos. Chem. Phys.*, 12, 779–799, <https://doi.org/10.5194/acp-12-779-2012>, 2012.
- Zhang, Y., Li, Z., Zhang, Y., Li, D., Qie, L., Che, H., and Xu, H.: Estimation of aerosol complex refractive indices for both fine and coarse modes simultaneously based on AERONET remote sensing products, *Atmos. Meas. Tech.*, 10, 3203–3213, <https://doi.org/10.5194/amt-10-3203-2017>, 2017.
- Zhang, Y., Li, Z., Sun, Y., Lv, Y., and Xie, Y.: Estimation of atmospheric columnar organic matter (OM) mass concentration from remote sensing measurements of aerosol spectral refractive indices, *Atmo. Environ.*, 179, 107–117, 2018.